Heliyon 10 (2024) e34344

Contents lists available at ScienceDirect

Heliyon

journal homepage: www.cell.com/heliyon

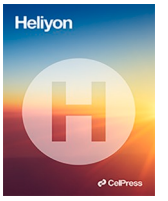

Research article

A novel endoscopic ultrasomics-based machine learning model and nomogram to predict the pathological grading of pancreatic neuroendocrine tumors

Shuangyang Mo [a,b,1], Yingwei Wang [b,1], Cheng Huang [c,1], Wenhong Wu [b], Shanyu Qin [a,*]

[a] Gastroenterology Department, The First Affiliated Hospital of Guangxi Medical University, Nanning, China
[b] Gastroenterology Department, Liuzhou People's Hospital Affiliated to Guangxi Medical University, Liuzhou, China
[c] Oncology Department, Liuzhou People's Hospital Affiliated to Guangxi Medical University, Liuzhou, China

ARTICLE INFO

Keywords:
Pancreatic neuroendocrine tumors
Endoscopic ultrasonography
Ulstrasomics
Machine learning
Pathology grading

ABSTRACT

Objectives: This research aimed to retrospectively construct and authenticate ultrasomics models using endoscopic ultrasonography (EUS) images for forecasting the pathological grading of pancreatic neuroendocrine tumors (PNETs).
Methods: After confirmation through pathological examination, a retrospective analysis of 79 patients was conducted, including 49 with grade 1 PNETs and 30 with grade 2/3 PNETs. These patients were randomized to the training or test cohort in a 6:4 proportion. The least absolute shrinkage and selection operator (LASSO) algorithm was used to reduce the dimensionality of ultrasomics features derived from standard EUS images. These nonzero coefficient features were retained and applied to construct prediction models via eight machine-learning algorithms. The optimum ulstrasomics model was determined, followed by creating and evaluating a nomogram.
Results: Ultrasomics features of 107 were extracted, and only those with coefficients greater than zero were retained. The XGboost ultrasomics model performed exceptionally well, achieving AUCs of 0.987 and 0.781 in the training and test cohorts, respectively. Furthermore, an effective nomogram was developed and visually represented. Finally, the calibration curves, decision curve analysis (DCA) plots, and clinical impact curve (CIC) displayed in the ulstrasomics model and nomogram demonstrated high accuracy. They provided significant net benefits for clinical decision-making.
Conclusions: A novel ulstrasomics model and nomogram were created and certified to predict the pathological grading of PNETs using EUS images. This study has the potential to provide valuable insights that improve the clinical applicability and efficacy of EUS in predicting the grading of PNETs.

1. Introduction

Pancreatic neuroendocrine tumors (PNETs) are uncommon neoplasms arising from the neuroendocrine cells of pancreatic islet

* Corresponding author.
E-mail address: qinshanyu@gxmu.edu.cn (S. Qin).
[1] Co-first authors.

https://doi.org/10.1016/j.heliyon.2024.e34344
Received 13 March 2024; Received in revised form 8 July 2024; Accepted 8 July 2024
Available online 9 July 2024

tissues, representing practically 1–3% of pancreatic neoplasms as a whole [1–3]. Recent reports indicate an increasing incidence of PNETs, due to the advancement of medical imaging modalities [4]. The 2022 World Health Organization (WHO) classifies PNETs as well-differentiated (grade 1, G1), intermediately differentiated (grade 2, G2), and poorly differentiated (grade 3, G3) tumors according to their mitotic rate and Ki-67 proliferation index [5]. The biological behavior of PNETs varies from low-level malignancy (G1) to hyperaggressive tumors (G3) [6]. Among PNETs, tumor grade is the most crucial prognostic determinant [7]. Previous studies indicated that Grade 2 non-functional PNETs should be considered high-risk [8]. In contrast, G1 asymptomatic and non-functional PNETs, particularly those with a diameter less than 2 cm, are advised to undergo active surveillance [9]. Contrarily, G2/3 PNETs are strongly correlated with worse prognoses and often require more intensive intervention [10]. Given the substantial impact of pathological grading on treatment decisions, the precise determination of PNETs grading is essential in clinical practice for optimal patient management [11,12]. Identifying and classifying G1 and G2/3 PNETs before surgical intervention poses a notable challenge. Currently, the predominant method for diagnosing and grading PNETs remains endoscopic ultrasonography-guided fine-needle aspiration/biopsy (EUS-FNA/B) despite its drawbacks, including invasiveness, limited accuracy, difficulty in capturing tumor heterogeneity, and a high technical barrier [13–15].

Many previous studies have revealed the application of magnetic resonance imaging (MRI), computed tomography (CT), and EUS to preoperatively predict the grading of PNETs [16–23]. However, the limited accuracy and/or deficient validation makes it hard to accomplish the diagnostic requirements [2]. A major benefit of EUS over other imaging modalities for pancreatic masses is its ability to produce high-resolution images [24]. Additionally, in 2023, the European Neuroendocrine Tumor Society (ENETS) established guidelines that recommended EUS as the preferred imaging procedure in cases where other noninvasive techniques yield inconclusive results [25]. EUS has demonstrated superior efficiency in the detection of PNETs compared to CT, MRI, and abdominal ultrasonography, especially for small lesions [26,27].

The combination of machine learning and radiomics methodologies has demonstrated encouraging outcomes in differentiating and prognosticating diverse cancer types [28]. Radiomics enables the extraction and evaluation of multiple quantitative image characteristics through high-throughput approaches [29]. Supervised learning, a subset of machine learning, involves training an artificial intelligence (AI) model using a labeled dataset in which the data is pre-categorized or labeled with correct responses. The model is subsequently trained to identify patterns within the data and generate predictions based on these patterns [30]. These supervised machine learning techniques, as well as LASSO regression analysis utilizing L1-normalization to penalize parameter weights and reduce dimensions, are commonly employed in radiomics research to screen relevant radiomics features and construct predictive models [31–34]. Previous studies have effectively utilized radiomics techniques on CT and MRI scans to predict the grading of PNETs, showcasing their remarkable efficacy [35–37]. Additionally, analysis of ultrasonic B-mode images has demonstrated the potential to

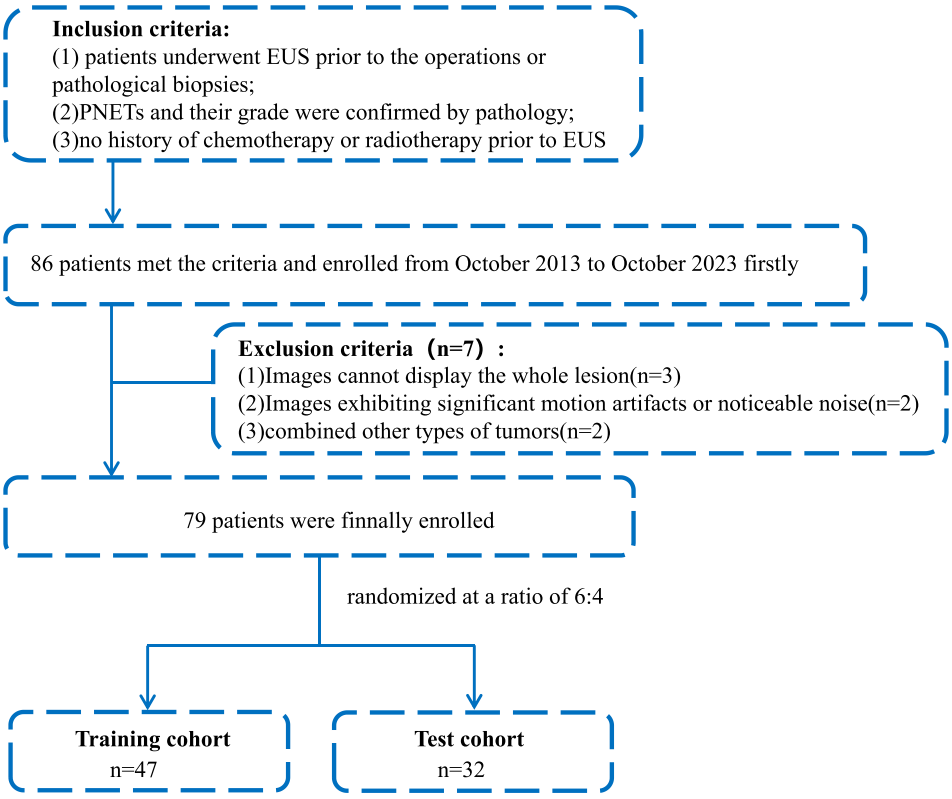

Fig. 1. Flowchart for enrolling the study population.

predict the pathological grade of PNETs based on ultrasomics features [38]. Nevertheless, the effectiveness and authenticity of EUS imaging-based ultrasomics in improving the predictive accuracy of preoperative grading of PNETs have not been established. Thus, this research sought to assess and validate the predictive potential of ultrasomics features derived from standard EUS images for classifying PNET grades.

2. Materials and methods

2.1. Study population

The institutional ethics review board of the First Affiliated Hospital of Guangxi Medical University approved this retrospective study (No. 2023-K346-01), thereby exempting the need for patient consent or signed informed consent for the examination of medical images and clinical information. A cohort of 79 participants with PNETs were enrolled in this study, including 49 individuals with G1 PNETs and 30 individuals with G2/3 PNETs, who underwent pancreatic surgery or endoscopic ultrasonography-guided fine-needle aspiration/biopsy (EUS-FNA/B) in our hospital during October 2013 and October 2023.

2.2. Herein are outlined the criteria for inclusion and exclusion

Patients were included based on the following criteria: (1) underwent meticulous EUS scanning of the pancreas before surgery; (2) had confirmed pathological grading; and (3) before preoperative or pathological biopsies, complete, clear EUS images were available; (4) before EUS, chemotherapy or radiotherapy could not be administered. Patients with tumors of other types, motion artifacts, or noise, or incapable of showing the entire lesion were excluded from the study. Training cohorts and test cohorts were randomized 6:4 among the registered individuals, as depicted in Fig. 1.

Analyzing various endoscopic ultrasonic features and clinical parameters, such as age, gender, location of the pancreatic mass, maximum diameter, shape, margin characteristics, echo characteristics, uniformity of echo, calcification, and cystic features, was carried out in this study, retrospectively.

2.3. EUS image acquisition

The research utilized the conventional dynamic EUS technique with the SU-9000 (FUJIFILM, Japan) and EU-ME2 (Olympus, Japan) equipment. A proficient EUS specialist, having conducted over 10000 EUS procedures, thoroughly examined the complete pancreatic area and captured clear images of the masses. A level of 125 grayscale values and a window of 250 grayscale values were consistently used in these images. The imaging data was obtained by accessing information from our institution's Picture Archive and Communication System (PACS).

2.4. ROI delineation

Two experienced EUS specialists used ITK-SNAP software (version 3.8.1, http://www.itksnap.org) to manually outline the region of interest (ROI) in the DICOM-formatted images. Discrepancies in the specialists' delineations were resolved through collaborative discussion and consensus. Subsequently, two specialists in consultation utilized the EUS macroscopic characteristics of pancreatic masses to predict the pathological grading of PNETs. The histopathological diagnoses of the patients were unknown to these specialists.

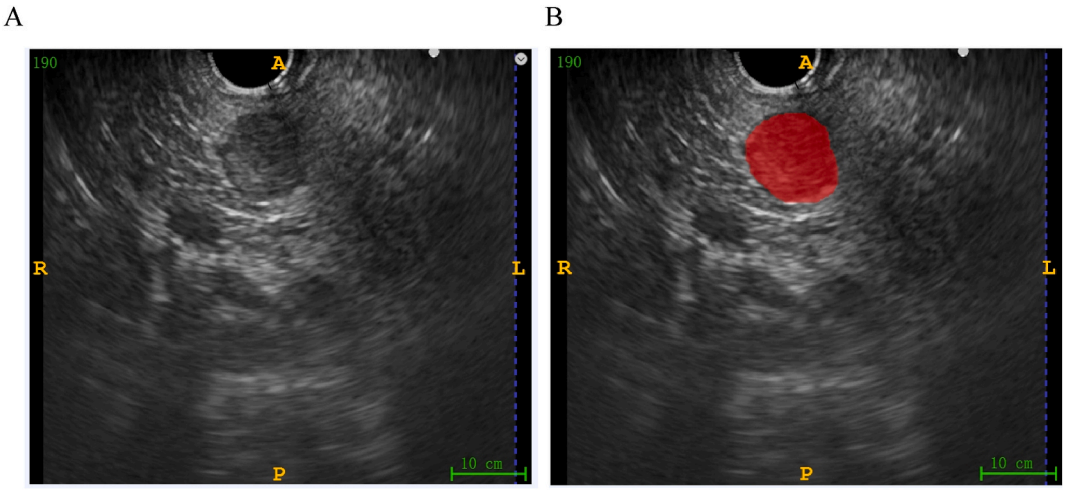

Fig. 2. Comprehensive graph of the region of interest (ROI).

On conventional EUS images, the lesions were meticulously delineated along their margins, excluding adjacent normal tissue, vessels, bile ducts, and pancreatic ducts. The diagram in Fig. 2 provides a comprehensive overview.

For reproducibility, standardization procedures were applied to the preprocessing of images and data. The intraclass correlation coefficient (ICC) was performed to estimate both intraobserver and interobserver reproducibility. Randomly selected 25 patients with G1 PNETs and 10 with G2/3 PNETs participated in the study. Following a one-month interval, the same EUS specialists performed ROI segmentation again. An ICC value greater than 0.8 signified a high level of agreement.

2.5. Ultrasomics feature extraction

The categorization of handcrafted features can be delineated into three discrete groups, namely intensity, geometric, and textural. The features of Geometric mainly focus on the shape of tumors, intensity features look at voxel intensity dispersion, and textural features analyze intensity patterns and spatial distributions. This study employed various methodologies, such as the gray level co-occurrence matrix (GLCM), gray level run length matrix (GLRLM), gray level size zone matrix (GLSZM), and neighborhood gray-level difference matrix (NGTDM), for the extraction of texture features from the ROI. The extraction of ultrasomics features adhered to the guidelines set forth by the Image Biomarker Standardization Initiative (IBSI) [39].

2.6. Ultrasomics feature selection

To evaluate the reliability of these ultrasomics features, a Mann–Whitney *U* test was performed to compare the training and test cohorts, followed by feature selection. Only ultrasomics features with a significance level of $p < 0.05$ were retained for further analysis. Spearman's rank correlation coefficient was employed to assess the interrelationships among features to verify their reliability. Features with a correlation coefficient exceeding 0.9 were preserved, and a greedy recursive deletion strategy was employed to enhance feature representation by iteratively removing the most redundant feature within the current set.

Consequently, a 10-fold cross-validation technique was utilized to identify features with nonzero coefficients through the application of the LASSO regression algorithm. The feature-selecting procedures were carried out within the training cohort and eventually implemented in the test cohort. Features with nonzero coefficients were preserved, conclusively. The Python scikit-learn package was utilized to perform the LASSO regression analysis.

A signature of ultrasomics was created by amalgamating features exhibiting nonzero coefficients. To determine the ultrasomics scores for each patient, a linear combination of the retained features and their corresponding model coefficients was applied.

2.7. Construction of ultrasomics models

Multiple prevailing machine learning algorithms were applied to construct categorization models for the superlative prediction of G1 and G2/3 PNETs.

After LASSO feature filtering was applied, commonly utilized supervised machine learning models, such as random forest (RF), logistic regression (LR), light gradient boosting machine (LightGBM), extreme gradient boosting (XGBoost), k nearest neighbors (KNN), support vector machine (SVM), extra tree, and multilayer perceptron (MLP), were performed to construct ultrasomics models, based on the retained ultrasomics features. The definitive ultrasomics signature was established by utilizing a 5-fold cross-validation technique.

Finally, the diagnostic performance of various machine learning algorithms was evaluated through the use of metrics. Eventually, the most superlative ultrasomics model was comprehensively identified.

2.8. Ultrasomics model assessment

The alignment between the prognostic forecasts generated by the optimal ultrasomics model and the actual results was assessed through the computation of the calibration curve, which juxtaposed the model's predictions against the theoretically perfect observations. The calibration efficacy of the optimal ultrasomics models was appraised by applying calibration curves and employing the Hosmer-Lemeshow (H-L) test to measure this efficacy. Furthermore, decision curve analysis (DCA) was utilized to assess the practical clinical value of this predictive model.

2.9. Ultrasomics nomogram establishment and assessment

The R rms package was employed in the development of an ultrasomics nomogram to assess the predictive utility of retained ultrasomics features in distinguishing between G1 and G2/3 PNETs intuitively and efficiently. The calibration curve was produced to confirm the calibration of the nomogram, utilizing mean absolute error and 1000 bootstrap samples. DCA and clinical impact curve (CIC) were further utilized to evaluate the net benefit and predictive performance of the nomogram, respectively.

2.10. Statistical analysis

A comparison of clinical parameters and ultrasomics features among participants was conducted using appropriate statistical tests such as independent sample *t*-test, Mann–Whitney *U* test, or X^2 test. Statistical significance was determined at a two-tailed p-value

<0.05. Prediction performance was evaluated based on metrics including area under the curve (AUC), specificity, sensitivity, accuracy, positive predictive value (PPV), and negative predictive value (NPV). The comprehensive methodology for this research is illustrated in Fig. 3.

3. Results

3.1. Clinical and baseline characteristics

This retrospective study included a group of 79 patients, with 47 women and 32 men, divided into training (N = 47) and test (N = 32) cohorts. Patients with G1 PNETs presented consistent characteristics of age, gender, echo characteristic, uniformity of echo, calcification, and location compared to those with G2/3 PNETs. Correspondingly, the results demonstrated notable differences in maximum diameter, margin characteristics, shape, and cystic degeneration between participants with G1 and G2/3 PNETs. Notably, G1 PNETs displayed a significantly smaller diameter, regular shape, clear margin, and less presence of cystic degeneration when compared to G2/3 PNETs (Table 1).

3.2. Univariate and multivariate logistic regression

Clinical and ultrasonic features were analyzed via univariate and multivariate methods. The significant features identified in the univariate analysis, including maximum diameter, shape, and margin characteristics, were further analyzed in the multivariate analysis. However, the multivariate logistic regression did not reveal any independent clinical and ultrasonic features that were significantly associated, indicating limited diagnostic performance based solely on the population and macroscopic EUS features (Table 2).

3.3. Ultrasomics feature extraction and screening

PyRadiomics, an internal feature analysis tool, was applied to extract all handcrafted features. A thorough analysis was conducted

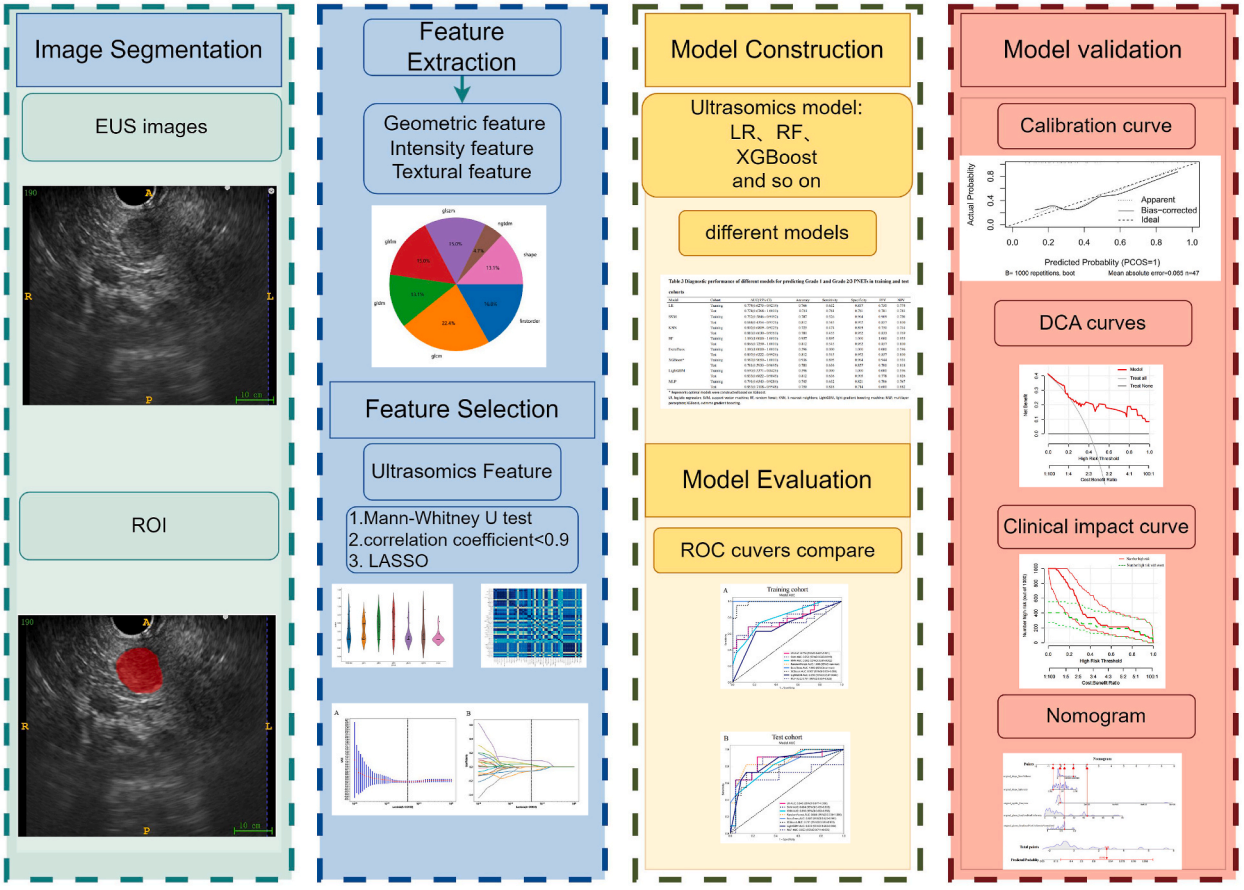

Fig. 3. The workflow of this study.

Table 1
Clinical and ultrasonic characteristics between the G1 and G2/3 groups.

Variable	Pathological Grades		
	G1	G2/3	*P*-value
Age	50.00 [37.00, 56.00]	50.50 [42.25, 62.25]	0.368
Maximum diameter	21.00 [13.40, 32.00]	34.85 [27.00, 47.50]	<0.001
Gender			0.524
0	31 (63.27 %)	16 (53.33 %)	
1	18 (36.73 %)	14 (46.67 %)	
Shape			<0.001
0	11 (22.45 %)	19 (63.33 %)	
1	38 (77.55 %)	11 (36.67 %)	
Margin			0.002
0	2 (4.08 %)	9 (30.00 %)	
1	47 (95.92 %)	21 (70.00 %)	
Echo			0.080
0	9 (18.37 %)	1 (3.33 %)	
1	40 (81.63 %)	29 (96.67 %)	
uniformity			0.110
0	24 (48.98 %)	21 (70.00 %)	
1	25 (51.02 %)	9 (30.00 %)	
Calcification			>0.999
0	48 (97.96 %)	29 (96.67 %)	
1	1 (2.04 %)	1 (3.33 %)	
Cystic areas			0.037
0	46 (93.88 %)	23 (76.67 %)	
1	3 (6.12 %)	7 (23.33 %)	
Location			
0	23 (46.94 %)	15 (50.00 %)	
1	26 (53.06 %)	15 (50.00 %)	

Gender: "0" means female, "1" means male; Shape: "0" means irregular shape, "1" means regular shape; Margin: "0" means unclear margin of lesion, "1" means clear margin of lesion; Echo: "0" means means not hypoechoic of lesion, "1" means hypoechoic of lesion; uniformity: "0" means nonuniformity of echo; "1" means uniformity of echo; Calcification: "0" means no calcification, "1" means calcification; Cystic areas: "0" means no cystic areas, "1" means cystic areas; Location: "0" means head and uncinate process of the pancreas, "1" means body and tail of the pancreas.

Table 2
Univariate and multivariable logistic regression analyses for selecting clinical and radiological features.

Variable	Univariate analysis		Multivariate analysis	
	OR (95 % CI)	*P*-value	OR(95 % CI)	*P*-value
Age	1.002(0.993, 1.011)	0.719		
Maximum diameter	1.011(1.003, 1.018)	0.028*	1.008(1.000,1.015)	0.090
Shape	0.711(0.563,0.899)	0.018*	0.833(0.645,1.075)	0.234
Margin	0.587(0.427,0.807)	0.007**	0.713(0.499,1.020)	0.120
Echo	1.184(0.763, 1.835)	0.522		
uniformity	0.822(0.647,1.046)	0.179		
Calcification	1.000(1.000,1.000)	NA		
Cystic areas	1.459(0.949, 2.243)	0.147		
Location	1.079(0.845,1.380)	0.604		
Gender	1.124(0.876,1.441)	0.435		

OR , odds ratio; CI, confidence interval.

to identify a total of 107 manually derived radiomic features across 7 categories, including 14 shape features, 18 first-order features, and the remaining texture features. Detailed definitions regarding these handcrafted features can be found in this literature [40].

Fig. 4a summarizes all ultrasomics features with their corresponding p-values. All ultrasomics features with *P* values less than 0.05, and their correlation coefficient heat maps are presented in Fig. 4b. Ultimately, five ultrasomics features with non-zero coefficients were identified. The coefficients and mean standard errors (MSEs) obtained from the 10-fold validation process are illustrated in Fig. 5a and b, respectively. In contrast, while the selected ultrasomics features with their corresponding coefficients are depicted in Fig. 5c. The optimal value of λ was found to be 0.0450, and subsequently, these five ultrasomics features were incorporated into a linear prediction model. The linear expression is as follows:

Ultrasomics Score = 0.379746835443038

+0.087928*original_glszm_SizeZoneNonUniformity

+0.032006 * original_ngtdm_Busyness

A

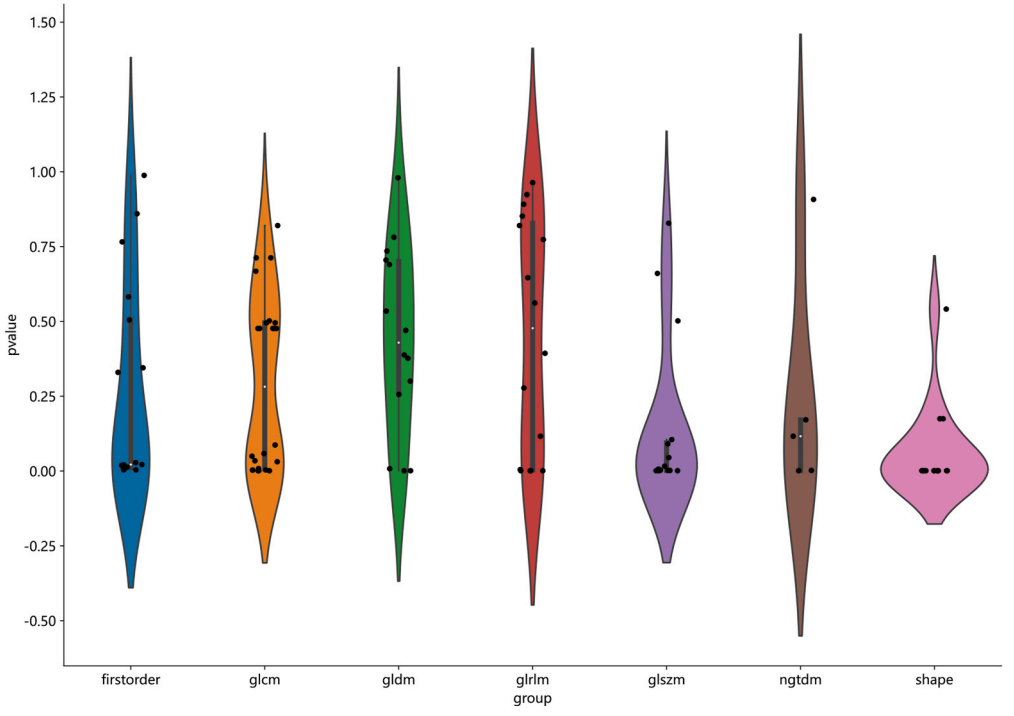

B

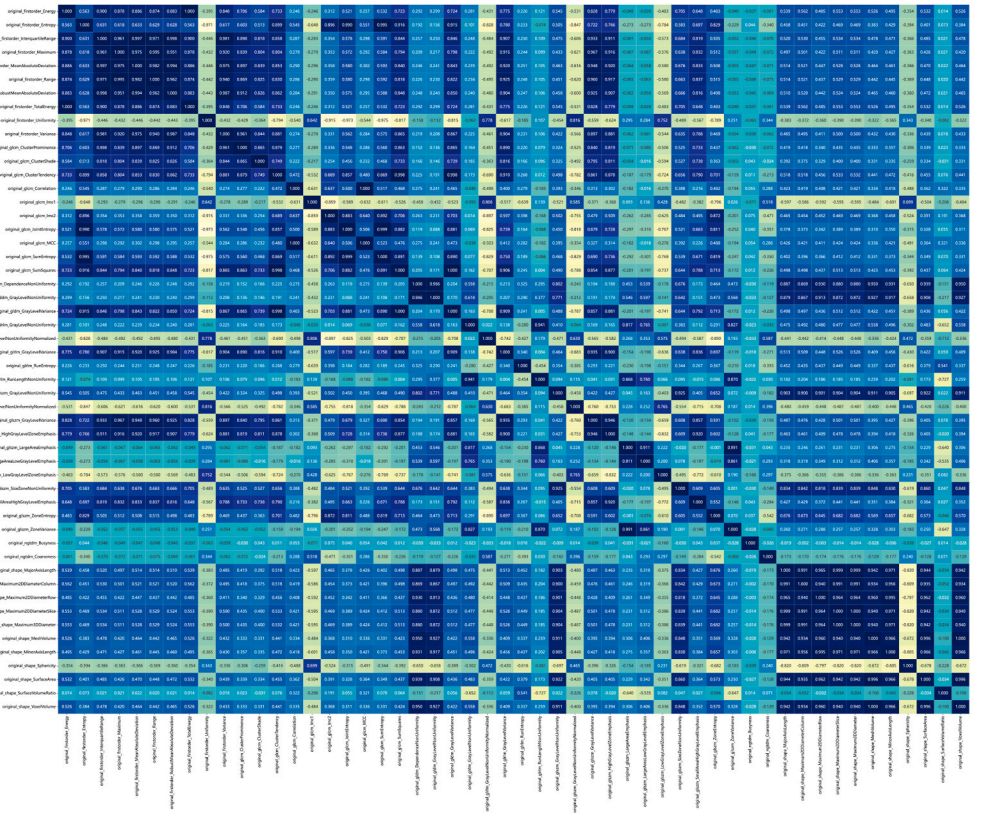

(caption on next page)

Fig. 4. **(A)**Violin plot for differential analyses of ultrasomics features with their corresponding *p* values. (**B**) Heat map of correlation coefficient of differential ultrasomics features.

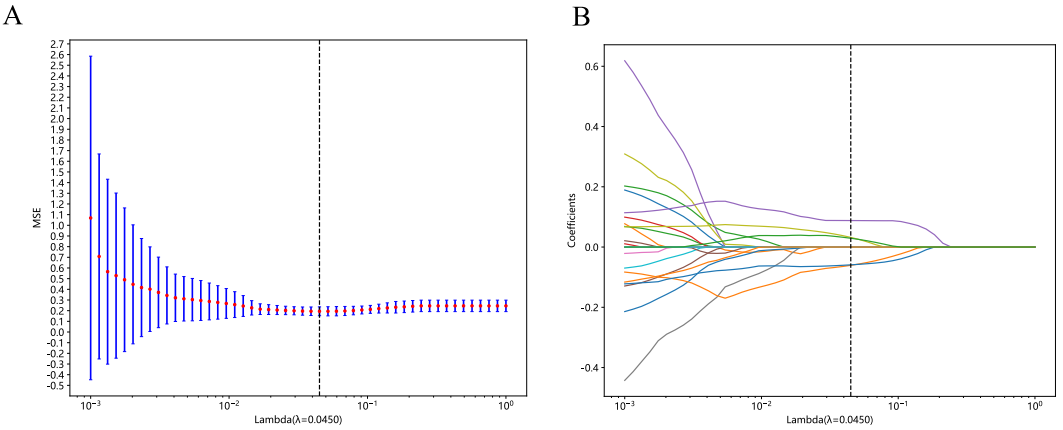

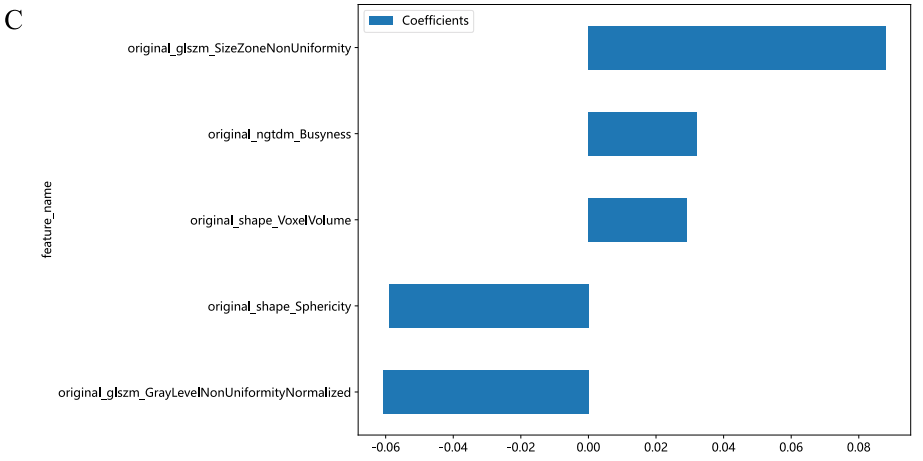

Fig. 5. Ultrasomics feature selection with the LASSO regression model. **(A)** The LASSO model's tuning parameter (λ) was selected using 10-fold cross-validation via the minimum criterion. The vertical lines illustrate the optimal value of the LASSO tuning parameter (λ) for the ultrasomics features. **(B)** A LASSO coefficient profile plot with different log(λ) values is displayed. The vertical dashed lines represent 5 ultrasomics features with nonzero coefficients selected with the optimal λ value. (**C**) The bar graph of ultrasomics features with their nonzero coefficients.

+0.029176 * original_shape_VoxelVolume

−0.059119 * original_shape_Sphericity

−0.060709*original_glszm_GrayLevelNonUniformityNormalized

3.4. Ultrasomics models and performance

As shown in Fig. 6a and b, the ROC curves and AUCs of each ultrasomics model derived from the eight widely used machine learning algorithms are shown for the training and test cohorts. A comprehensive overview of the results can be found in Table 3. Note that the RF and ExtraTrees models have a clear tendency to overfit. The AUCs of the LR model, the KNN model, the LightGBM model, and the MLP model in the test cohort exceeded those in the training cohort, which was both inaccurate and unobjective. Comparatively, the XGBoost model displayed better performance and showed stronger consistency between training (AUC = 0.987, 95 % CI

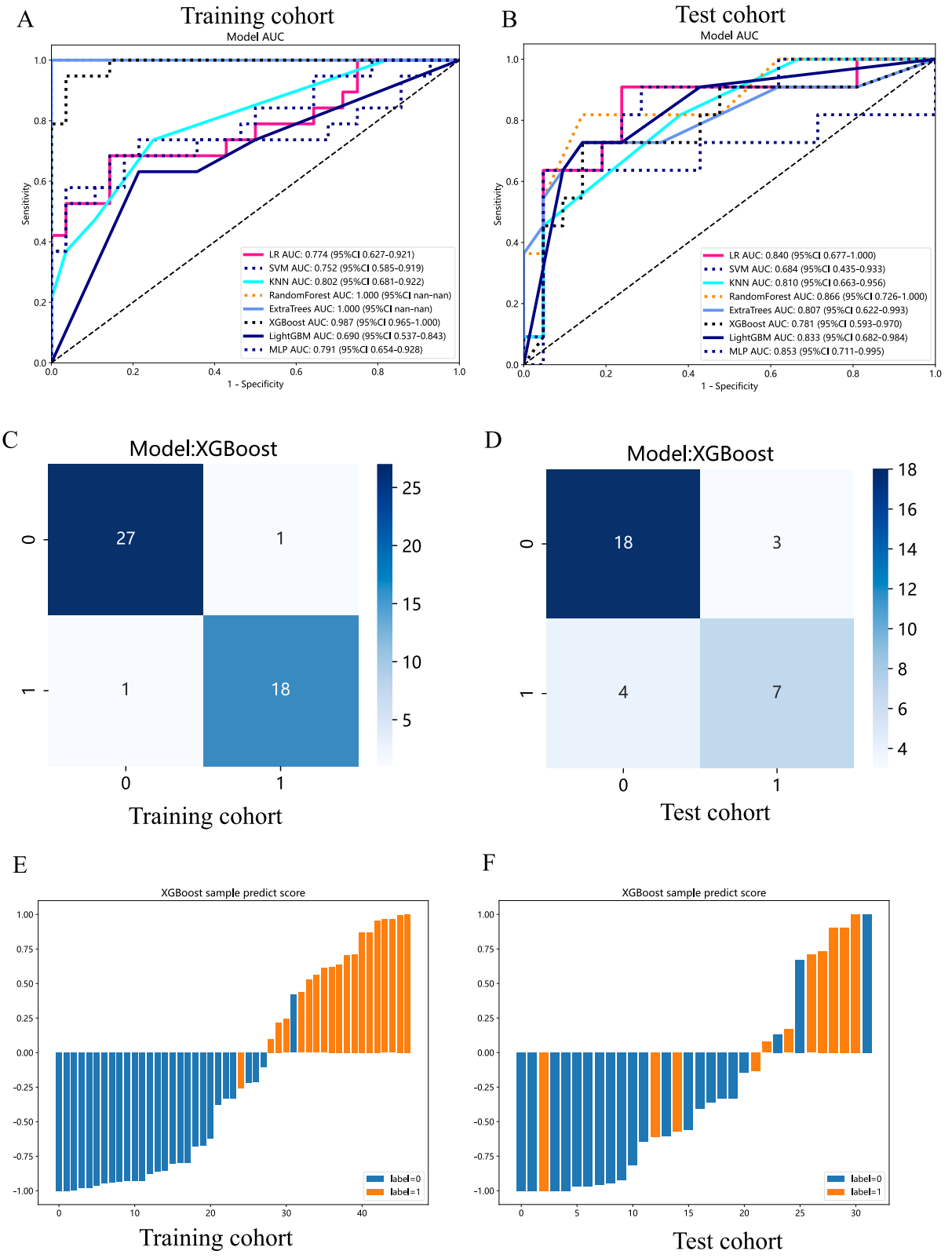

(caption on next page)

Fig. 6. **(A)**The ROC curves of different ultrasomics models based on eight machine learning algorithms for predicting G2/3 PNETs in the training cohort. (**B**) The ROC curves of different ultrasomics models in the test cohort. (**C**) The confusion matrix of the XGboost-based ultrasomics model in the training cohort. (**D**) The confusion matrix of the XGboost -based ultrasomics model in the test cohort. (**E**) XGboost-based prediction scores of the ultrasomics model in the training cohorts. (**F**) XGboost-based prediction scores of the ultrasomics model in the test cohorts. ("label = 0" means "G1 PNETs"; "label = 1" means "G2/3 PNETs").

Table 3
Diagnostic performance of different models for predicting Grade 1 and Grade 2/3 PNETs in training and test cohorts.

Model	Cohort	AUC(95 % CI)	Accuracy	Sensitivity	Specificity	PPV	NPV
LR	Training	0.774(0.6275–0.9214)	0.766	0.632	0.857	0.750	0.774
	Test	0.840(0.6768–1.0000)	0.781	0.781	0.781	0.781	0.781
SVM	Training	0.752(0.5846–0.9192)	0.787	0.526	0.964	0.909	0.750
	Test	0.684(0.4354–0.9326)	0.812	0.545	0.952	0.857	0.800
KNN	Training	0.802(0.6809–0.9225)	0.723	0.474	0.893	0.750	0.714
	Test	0.810(0.6630–0.9560)	0.781	0.455	0.952	0.833	0.769
RF	Training	1.000(1.0000–1.0000)	0.957	0.895	1.000	1.000	0.933
	Test	0.866(0.7259–1.0000)	0.812	0.545	0.952	0.857	0.800
ExtraTrees	Training	1.000(1.0000–1.0000)	0.596	0.000	1.000	0.000	0.596
	Test	0.807(0.6222–0.9926)	0.812	0.545	0.952	0.857	0.800
XGBoost[a]	Training	0.987(0.9650–1.0000)	0.936	0.895	0.964	0.944	0.931
	Test	0.781(0.5933–0.9695)	0.781	0.636	0.857	0.700	0.818
LightGBM	Training	0.690(0.5371–0.8426)	0.596	0.000	1.000	0.000	0.596
	Test	0.833(0.6822–0.9845)	0.812	0.636	0.905	0.778	0.826
MLP	Training	0.791(0.6543–0.9284)	0.745	0.632	0.821	0.706	0.767
	Test	0.853(0.7108–0.9948)	0.750	0.818	0.714	0.600	0.882

LR, logistic regression; SVM, support vector machine; RF, random forest; KNN, k nearest neighbors; LightGBM, light gradient boosting machine; MLP, multilayer perceptron; XGBoost, extreme gradient boosting.
[a] Represents optimal models were constructed based on XGBoost.

0.9650–1.0000) and test cohorts (AUC = 0.781, 95 % CI 0.5933–0.9695). Furthermore, the XGBoost model performed better in both training and test cohorts than the SVM model, demonstrating its effectiveness as an ultrasomics model. The XGBoost model demonstrated an accuracy of 0.781, sensitivity of 0.636, specificity of 0.857, positive predictive value PPV of 0.700, and NPV of 0.818 in the test cohort (Table 3). As a consequence, the XGBoost model was deemed appropriate for further analyses and chosen as the foundational model. The XGBoost model's prediction accuracy was demonstrated through the use of a confusion matrix (Fig. 6c and d), which accurately predicted the pathological grades of 45 cases (45/47) and 25 (25/32) cases of PNETs in the training and test cohorts, respectively. The prediction scores of the XGBoost-based ultransomics model are shown in Fig. 6e and f. Following consultation, the two specialists utilized macroscopic features observed through EUS to predict the pathological grading of PNETs. This approach successfully predicted the pathological grades of 28 out of 47 PNETs in the training cohort and 17 out of 32 PNETs in the test cohort. According to the data presented in Table 4, the XGBoost-based ultransomics model demonstrated a notably superior accuracy in predicting the pathological grading of PNETs compared to EUS specialists in both the training and test cohorts.

Furthermore, the ROC curve of the XGboost model is displayed in Fig. 7a. An illustration of the ultrasomics features retained in the XGboost models is shown in Fig. 7b.

Both the calibration curves of the XGboost model and perfectly calibrated G2/3 PNETs in the test and training cohorts showed remarkable consistency (Fig. 7c and d). The calibrations were confirmed by the H-L test. Finally, DCA was performed to evaluate XGboost's performance, as shown in Fig. 7e and f. Compared to hypothetical scenarios where there was no prediction model available, such as the treat-all or treat-none approaches, the XGboost model demonstrated a notable net benefit for patient intervention in both (Fig. 7e) and test (Fig. 7f) cohorts.

3.5. Construction and validation of ultrasomics nomogram

A nomogram was constructed to represent the five selected ultrasomics features with non-zero coefficients and facilitate clinical application (Fig. 8). Subsequently, the nomogram model was then evaluated with a calibration curve. With a mean absolute error of

Table 4
Comparison of the prediction accuracy of pathological grading of PNETs between XGBoost model and EUS specialists.

Model	Training cohort(N = 47)		Test cohort (N = 32)	
	Correct	Incorrect	Correct	Incorrect
XGboost	45(95.74 %)	2 (4.26 %)	25(78.13 %)	7(21.87 %)
EUS specialists	28(59.57 %)	19(40.43 %)	17(53.13 %)	15(46.87 %)
X^2	17.7208		4.4329	
P-value	<0.0001		0.0353	

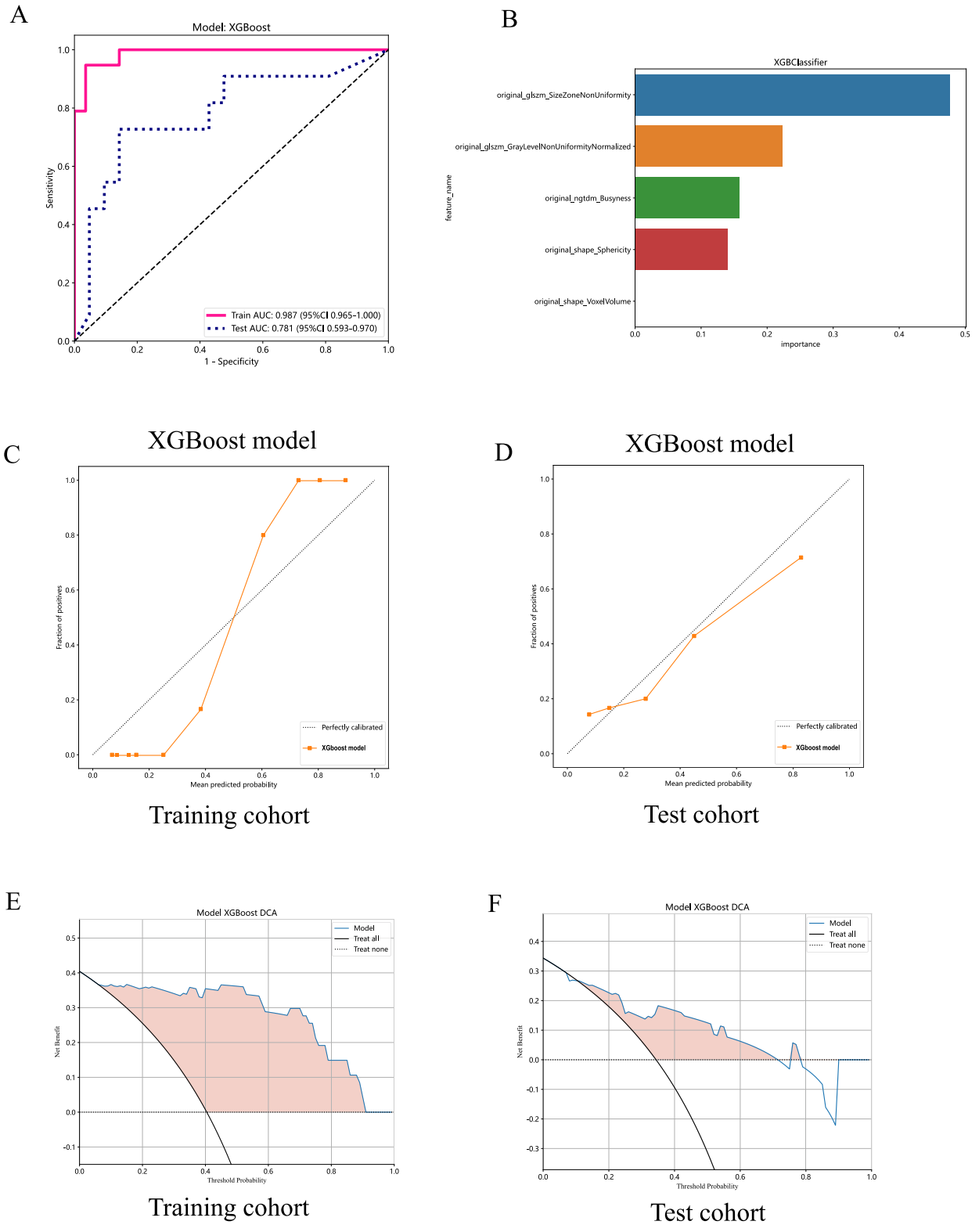

Fig. 7. **(A)**The ROC curves of the ultrasomics model based on XGboost in both the training and test cohorts. **(B)** The weight bars graph of the retained ultrasomics features in the XGboost model. **(C-D)** Calibration curve for the ultrasomics model based on XGboost in the training **(C)** and test **(D)** cohort. **(E-F)** The DCA curves for the ultrasomics model based on XGboost in the training (**E**) and test (**F**) cohorts.

0.059, the calibration curve revealed that the error between the predicted and actual probability of G2/3 PNETs is extremely negligible in the training cohort (Fig. 9a). Additionally, As shown in Fig. 9b, this nomogram model offers outstanding net benefits. As displayed in the CIC (Fig. 9c), it demonstrated that this nomogram model exhibited extraordinary performance for G2/3 PNETs prediction. Similarly, the test cohort showed highly analogous performances for this nomogram (Fig. 10a, b, and c).

4. Discussion

This study constructed various models for predicting the pathological grading of PNETs by combining EUS-based ultrasomics features with eight machine-learning algorithms based on ROI data. Results from our investigation revealed that combining endoscopic ultrasomics features and machine learning yielded remarkably accurate prediction performance for G2/3 PNETs, especially the XGboost model demonstrated high-performance metrics in the training (AUC = 0.987, 95 % CI 0.9650–1.0000) and test (AUC = 0.781, 95 % CI 0.5933–0.9695) cohorts. Additionally, the nonzero-coefficient ultrasomics features were utilized to develop a nomogram for predicting G2/3 PNETs, which exhibited exceptional efficacy and accuracy in both training and test cohorts as evidenced by calibration curves, DCA curves, and CICs. Thus, it was deemed a dependable and valid instrument for predicting grades of PNETs and guiding treatment decisions. These results indicate that EUS ultrasomics features may offer additional diagnostic information to improve the detection of G2/3 PNETs. Similarly, it has previously been shown that deep learning contrast-enhanced ultrasound combined with clinical characteristics is effective in identifying preoperative aggressiveness in PNETs [41]. Additionally, previous research has demonstrated that EUS imaging can be used to detect gastrointestinal stromal tumors and pancreatic ductal adenocarcinomas by using ultrasomics, machine learning, and deep learning methods [29,42,43]. However, this is the first investigation to report that a novel model and nomogram based on EUS imaging are capable of predicting PNETs grading with remarkable accuracy, as far as our knowledge extends.

Many previous researches have assessed the potential association between medical imaging characteristics and PNETs grading. Zhu H demonstrated that a well-defined margin on the EUS image was mostly associated with lower pathological grade [22]. Similarly, A study indicated that obscure boundaries were more common in G2/3 PNETs with a high specificity of 90.3 % [16]. Claudio R found that the diameter of tumors was positively correlated with the risk of G2/3 PNETs [44]. A high-grade malignancy and a poor prognosis are closely associated with cystic degeneration, calcification, and necrosis [45,46]. Toshima F's research revealed a significant connection between calcification, cystic degeneration, and necrosis and the likelihood of high-grade malignancy and unfavorable outcomes in individuals with PNETs. Utilizing univariate analysis, Toshima F found that tumor shape, maximum size, and cystic degeneration were predictive factors for distinguishing between G1/2 and G3 PNETs. Furthermore, multivariate regression analysis indicated that the presence of an irregular lobulated mass was suggestive of a G3 tumor diagnosis [47].

The findings of our study demonstrate a significant association between larger maximum diameter, irregular shape, and unclear margin with G2/3 PNETs based on univariate analysis, in line with existing literature [48]. However, multivariate logistic regression analysis did not identify any EUS macroscopic characteristics as independent risk factors for predicting tumor grading. Significantly, while preoperative EUS imaging has shown effectiveness in assessing the characteristics and proximity of functional PNETs [49],

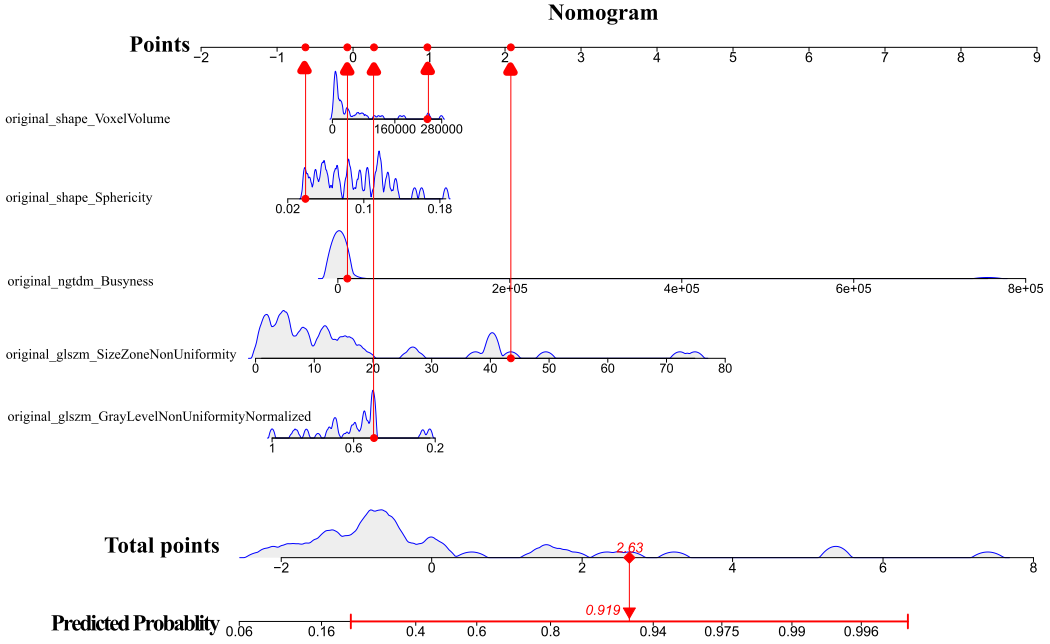

Fig. 8. The Nomogram for predicting G2/3 PNETs based on five retained ultrasomics features. The nomogram is used by summing all points identified on the scale for each variable. The total points projected on the bottom scales indicate the probabilities of G2/3 PNETs.

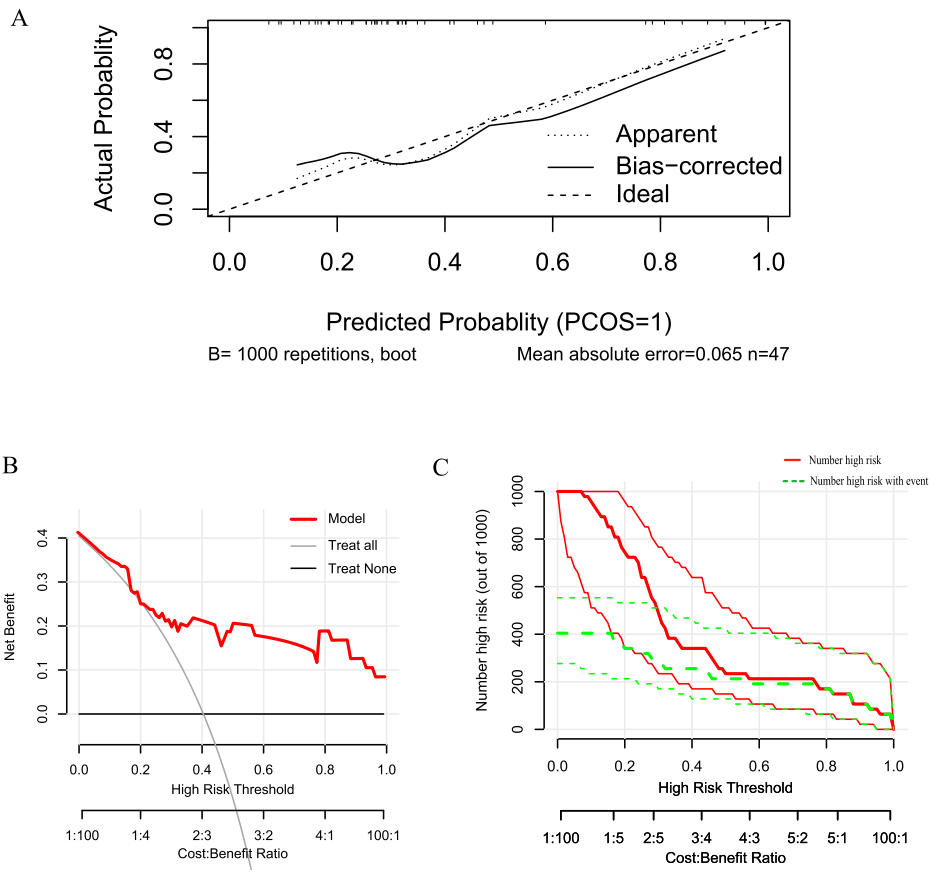

Fig. 9. **(A)** The calibration curves for the nomogram with the mean absolute error = 0.065 in the training cohort. **(B)** DCA of the nomogram in the training cohort ("Treat all" means diagnosis-all strategy; "Treat none" means diagnosis-none strategy). **(C)**The CIC of the nomogram in the training cohort.

EUS currently differentiates pancreatic masses predominantly based on macroscopic anatomical features. This reliance on anatomical characteristics results in insufficient specificity and the risk of subjective interpretation. Furthermore, the limited enrollment of small-scale populations and the utilization of subjective features in these studies may be attributed to the low incidence and challenges in grading PNETs. Thus, a reliable approach that can preoperatively promote grading prediction of PNETs is an imperative need.

Medical imaging can be analyzed in a way that is more efficient and accurate than visual diagnosis, thanks to radiomics. It can improve the accuracy of predictive models for different tumor types, allowing more accurate cancer diagnoses [50–52]. Non-contrast MRI radiomics and combined models demonstrated superior predictive ability to distinguish G1 and G2/3 NF-PNETs, outperforming models based on clinical and radiological features in a multicenter study [53]. Additionally, Gu D's research illustrated that radiomic signatures derived from CT imaging are more accurate in predicting the pathological grading of PNETs [2]. Similarly, Bian Y conducted a study utilizing non-contrast MRI and developed an effective radiomics model to differentiate between G1 and G2/3 tumors and facilitate clinical decision-making [35]. In a recent study, MRI and contrast-enhanced CT features were incorporated into a composite model, which showed improved predictive performance for grading PNETs in both the training (AUC = 0.92) and validation (AUC = 0.85) cohorts compared to single-modality radiomics models [54]. We found that EUS image-based ulstrasomics models and nomograms are precise and effective for predicting PNET grading, similar to previous literature.

In this research, a total of 107 ultrasomics features were reduced to five potential predictors for the development of the ultrasomics model. The most influential ultrasomics predictor, with the highest weight in the XGboost model, is a GLSZM-based feature known as "Size Zone Non-uniformity". Previous studies have indicated that GLSZM features derived from MRI images exhibit varying levels of robustness in the segmentation of gliomas [55]. Another study demonstrated that texture features, particularly GLSZM, were important markers for distinguishing non-small cell lung cancer subtypes [56]. An investigation of the correlation between GLSZM features and histopathology grading is needed. Battistella Anna noted that tumors with low micro-vessel density could indicate high aggressiveness in patients with non-functional PNETs [57], suggesting a potential explanation for this phenomenon.

While the ultrasomics model and nomogram utilizing EUS imaging showed significant efficacy, this study is limited by various factors. It is possible to introduce selection bias into retrospective analyses conducted at one center, and bias may also be present in the

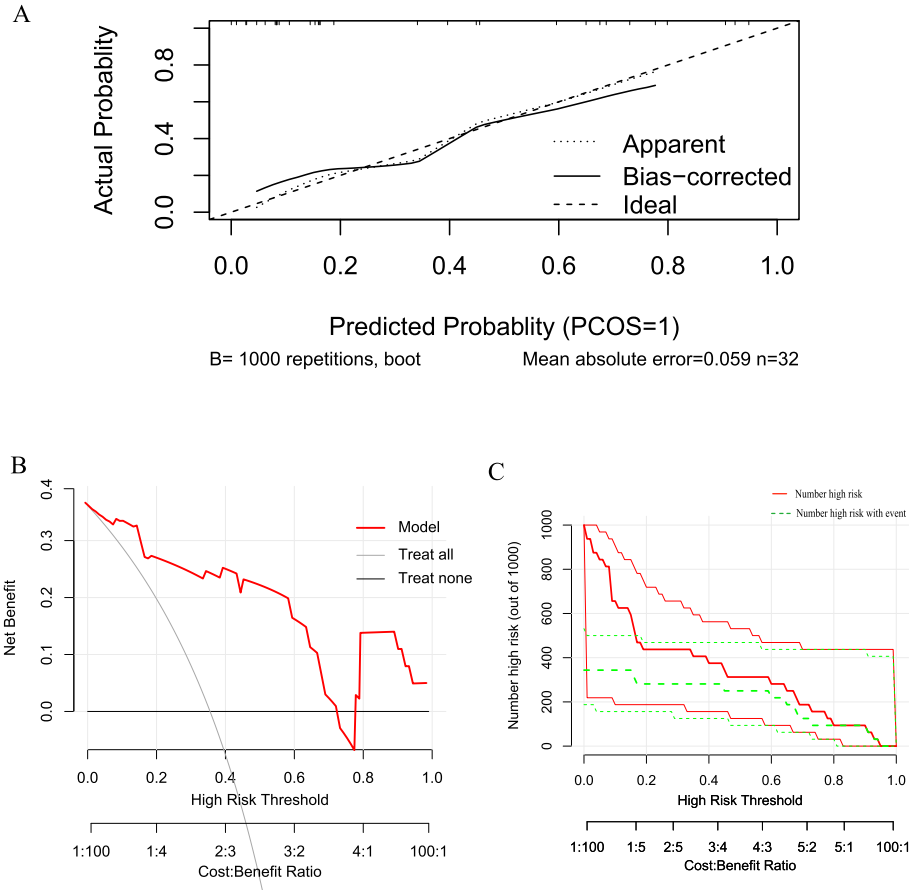

Fig. 10. **(A)** The calibration curves for the nomogram with the mean absolute error = 0.059 in the test cohort. **(B)** DCA of the nomogram in the test cohort ("Treat all" means diagnosis-all strategy; "Treat none" means diagnosis-none strategy). **(C)**The CIC of the nomogram in the test cohort.

image segmentation process due to manual segmentation [58]. Additionally, we used EUS imaging with two heterogeneous devices from two different companies, which may cause potential noise and bias, although stand standardization procedures were applied. Ultimately, the limited sample size, particularly among patients with G3 PNETs. Thus, the importance of encompassing multiple centers, large sample sizes, prospective designs, and multimodal approaches for future EUS-based ultrasomics research for the grading of PNETs might be imperative. Additionally, integrating deep learning methodologies and exploring the underlying biological changes in peritumor imaging characteristics could mitigate bias and enhance the interpretability of the models.

5. Conclusion

In conclusion, a novel ulstrasomics model and visual nomogram based on EUS images were constructed and validated, incorporating machine learning algorithms. A comparison of different machine learning algorithms revealed that the XGboost model demonstrated the most favorable diagnostic efficacy. There is encouraging potential for promoting the clinical applicability of EUS in predicting PNETs grading, providing valuable perceptions for future study and implementation.

Data availability

Detailed contributions to the study are included in the article/supplements; corresponding authors can be contacted for further inquiries.

Code availability

The inquiry of the original code for this manuscript can be directed to the corresponding authors.

Funding

This study was supported by the Scientific Research Project of Liuzhou People's Hospital affiliated with Guangxi Medical University, China (grant numbers: lry202309 and lry202311), the Scientific Research Project of Guangxi Health Commission, China (grant number: Z-B20231296, Z-B20231339, Z20200113).

Ethics approval and consent to participate

Following the Declaration of Helsinki, this retrospective study was approved by the Medical Ethics Committee of The First Affiliated Hospital of Guangxi Medical University (No. 2023-K346-01, 2023-12-29), China. Considering the retrospective nature of the study, informed consent was not required.

Consent for publication

Not applicable.

CRediT authorship contribution statement

Shuangyang Mo: Writing – review & editing, Writing – original draft, Visualization, Validation, Supervision, Software, Resources, Project administration, Methodology, Investigation, Funding acquisition, Formal analysis, Data curation. **Yingwei Wang:** Writing – original draft, Visualization, Validation, Supervision, Software, Resources, Formal analysis. **Cheng Huang:** Writing – original draft, Visualization, Validation, Software, Methodology, Investigation, Formal analysis, Data curation, Conceptualization. **Wenhong Wu:** Visualization, Software, Resources, Project administration, Methodology, Investigation. **Shanyu Qin:** Writing – review & editing, Writing – original draft, Visualization, Validation, Supervision, Software, Resources, Project administration, Methodology, Investigation, Formal analysis, Data curation, Conceptualization.

Declaration of competing interest

The authors declare the following financial interests/personal relationships which may be considered as potential competing interests:Mo shuangyang reports administrative support was provided by Guangxi Health Commission. If there are other authors, they declare that they have no known competing financial interests or personal relationships that could have appeared to influence the work reported in this paper.

Acknowledgements

The Onekey platform and its developers deserve our appreciation.

References

[1] Y. Bian, J. Li, H. Jiang, X. Fang, K. Cao, C. Ma, J. Lu, Tumor size on microscopy, CT, and MRI Assessments versus pathologic Gross Specimen analysis of pancreatic neuroendocrine tumors. AJR, Am. J. Roentgenol. 217 (2021) 107–116.
[2] D. Gu, Y. Hu, H. Ding, J. Wei, K. Chen, H. Liu, M. Zeng, J. Tian, CT radiomics may predict the grade of pancreatic neuroendocrine tumors: a multicenter study, Eur. Radiol. 29 (2019) 6880–6890.
[3] R. Souche, C. Hobeika, E. Hain, S. Gaujoux, Surgical management of neuroendocrine tumours of the pancreas, J. Clin. Med. 9 (2020).
[4] I.W. Han, J. Park, E.Y. Park, S.J. Yoon, G. Jin, D.W. Hwang, K. Jiang, W. Kwon, X. Xu, J.S. Heo, D.L. Fu, W.J. Lee, X. Bai, Y.S. Yoon, Y.M. Yang, K.S. Ahn, C. Yuan, H.K. Lee, B. Sun, E.K. Park, S.E. Lee, S. Kang, W. Lou, S.J. Park, Fate of surgical patients with small nonfunctioning pancreatic neuroendocrine tumors: an international study using multi-institutional registries, Cancers 14 (2022).
[5] O. Buchstab, T. Knösel, [Current WHO Classification (2022) of Neuroendocrine Neoplasms], Radiologie, Heidelberg, Germany, 2024.
[6] Z. Tong, L. Wang, W. Shi, Y. Zeng, H. Zhang, L. Liu, Y. Zheng, C. Chen, W. Xia, W. Fang, P. Zhao, Clonal evolution dynamics in primary and metastatic lesions of pancreatic neuroendocrine neoplasms, Front. Med. 8 (2021) 620988.
[7] M. D'Onofrio, V. Ciaravino, N. Cardobi, R. De Robertis, S. Cingarlini, L. Landoni, P. Capelli, C. Bassi, A. Scarpa, CT enhancement and 3D texture analysis of pancreatic neuroendocrine neoplasms, Sci. Rep. 9 (2019) 2176.
[8] S.M. Sadowski, C.R.C. Pieterman, N.D. Perrier, F. Triponez, G.D. Valk, Prognostic factors for the outcome of nonfunctioning pancreatic neuroendocrine tumors in MEN1: a systematic review of literature, Endocr. Relat. Cancer 27 (2020) R145–r161.
[9] S. Partelli, S. Massironi, A. Zerbi, P. Niccoli, W. Kwon, L. Landoni, F. Panzuto, A. Tomazic, A. Bongiovanni, G. Kaltsas, A. Sauvanet, E. Bertani, V. Mazzaferro, M. Caplin, T. Armstrong, M.O. Weickert, J. Ramage, E. Segelov, G. Butturini, S. Staettner, M. Cives, A. Frilling, C.A. Moulton, J. He, F. Boesch, A. Selberheer, O. Twito, A. Castaldi, C.G. De Angelis, S. Gaujoux, K. Holzer, C.H. Wilson, H. Almeamar, E. Vigia, F. Muffatti, M. Lucà, A. Lania, J. Ewald, H. Kim, R. Salvia, M. Rinzivillo, A. Smid, A. Gardini, M. Tsoli, O. Hentic, S. Colombo, D. Citterio, C. Toumpanakis, E. Ramsey, H.S. Randeva, R. Srirajaskanthan, D. Croagh, P. Regi, S. Gasteiger, P. Invernizzi, C. Ridolfi, M. Giovannini, J.Y. Jang, C. Bassi, M. Falconi, Management of asymptomatic sporadic non-functioning pancreatic neuroendocrine neoplasms no larger than 2 cm: interim analysis of prospective ASPEN trial, Br. J. Surg. 109 (2022) 1186–1190.
[10] R. Zheng-Pywell, A. Fang, A. AlKashash, S. Awad, S. Reddy, S. Vickers, M. Heslin, V. Dudeja, H. Chen, J.B. Rose, Prognostic impact of tumor size on pancreatic neuroendocrine tumor recurrence may have racial variance, Pancreas 50 (2021) 347–352.
[11] Y. Bian, H. Jiang, C. Ma, L. Wang, J. Zheng, G. Jin, J. Lu, CT-based radiomics score for distinguishing between grade 1 and grade 2 nonfunctioning pancreatic neuroendocrine tumors. AJR, Am. J. Roentgenol. 215 (2020) 852–863.
[12] H.B. Zhu, H.T. Zhu, L. Jiang, P. Nie, J. Hu, W. Tang, X.Y. Zhang, X.T. Li, Q. Yao, Y.S. Sun, Radiomics analysis from magnetic resonance imaging in predicting the grade of nonfunctioning pancreatic neuroendocrine tumors: a multicenter study, Eur. Radiol. 34 (2024) 90–102.

[13] M. Di Leo, L. Poliani, D. Rahal, F. Auriemma, A. Anderloni, C. Ridolfi, P. Spaggiari, G. Capretti, L. Di Tommaso, P. Preatoni, A. Zerbi, C. Carnaghi, A. Lania, A. Malesci, A. Repici, S. Carrara, Pancreatic neuroendocrine tumours: the role of endoscopic ultrasound biopsy in diagnosis and grading based on the WHO 2017 classification, Dig. Dis. 37 (2019) 325–333.
[14] C. Grosse, P. Noack, R. Silye, Accuracy of grading pancreatic neuroendocrine neoplasms with Ki-67 index in fine-needle aspiration cellblock material, Cytopathology : official journal of the British Society for Clinical Cytology 30 (2019) 187–193.
[15] S. Paiella, L. Landoni, R. Rota, M. Valenti, G. Elio, S.F. Crinò, E. Manfrin, A. Parisi, S. Cingarlini, M. D'Onofrio, A. Scarpa, R.T. Lawlor, L. Bernardoni, P. Capelli, C. Nessi, M. Miotto, A. Gabbrielli, C. Bassi, R. Salvia, Endoscopic ultrasound-guided fine-needle aspiration for the diagnosis and grading of pancreatic neuroendocrine tumors: a retrospective analysis of 110 cases, Endoscopy 52 (2020) 988–994.
[16] R. De Robertis, S. Cingarlini, P. Tinazzi Martini, S. Ortolani, G. Butturini, L. Landoni, P. Regi, R. Girelli, P. Capelli, S. Gobbo, G. Tortora, A. Scarpa, P. Pederzoli, M. D'Onofrio, Pancreatic neuroendocrine neoplasms: magnetic resonance imaging features according to grade and stage, World J. Gastroenterol. 23 (2017) 275–285.
[17] K.M. Jang, S.H. Kim, S.J. Lee, D. Choi, The value of gadoxetic acid-enhanced and diffusion-weighted MRI for prediction of grading of pancreatic neuroendocrine tumors, Acta Radiol. (Stockh.) 55 (2014) 140–148.
[18] E. Belousova, G. Karmazanovsky, A. Kriger, D. Kalinin, L. Mannelli, A. Glotov, N. Karelskaya, O. Paklina, A. Kaldarov, Contrast-enhanced MDCT in patients with pancreatic neuroendocrine tumours: correlation with histological findings and diagnostic performance in differentiation between tumour grades, Clin. Radiol. 72 (2017) 150–158.
[19] R. Canellas, K.S. Burk, A. Parakh, D.V. Sahani, Prediction of pancreatic neuroendocrine tumor grade based on CT features and texture analysis, AJR. American journal of roentgenology 210 (2018) 341–346.
[20] J. Kang, J.K. Ryu, J.H. Son, J.W. Lee, J.H. Choi, S.H. Lee, Y.T. Kim, Association between pathologic grade and multiphase computed tomography enhancement in pancreatic neuroendocrine neoplasm, J. Gastroenterol. Hepatol (2018). Published online March 7, 2018.
[21] R. De Robertis, B. Maris, N. Cardobi, P. Tinazzi Martini, S. Gobbo, P. Capelli, S. Ortolani, S. Cingarlini, S. Paiella, L. Landoni, G. Butturini, P. Regi, A. Scarpa, G. Tortora, M. D'Onofrio, Can histogram analysis of MR images predict aggressiveness in pancreatic neuroendocrine tumors? Eur. Radiol. 28 (2018) 2582–2591.
[22] H. Zhu, L. Ying, W. Tang, X. Yang, B. Sun, Can MDCT or EUS features predict the histopathological grading scheme of pancreatic neuroendocrine neoplasms? La Radiologia medica 122 (2017) 319–326.
[23] G. Franchellucci, M. Andreozzi, S. Carrara, L. De Luca, F. Auriemma, D. Paduano, F. Calabrese, A. Facciorusso, V. Poletti, A. Zerbi, A.G. Lania, A.F. Bertuzzi, P. Spaggiari, V. Pedicini, M. Rodari, P. Fusaroli, A. Lisotti, A. Ofosu, A. Repici, B. Mangiavillano, Contrast enhanced EUS for predicting solid pancreatic neuroendocrine tumor grade and aggressiveness, Diagnostics 13 (2023).
[24] G. Melita, S. Pallio, A. Tortora, S.F. Crinò, A. Macrì, G. Dionigi, Diagnostic and interventional role of endoscopic ultrasonography for the management of pancreatic neuroendocrine neoplasms, J. Clin. Med. 10 (2021).
[25] J. Hofland, M. Falconi, E. Christ, J.P. Castaño, A. Faggiano, A. Lamarca, A. Perren, S. Petrucci, V. Prasad, P. Ruszniewski, C. Thirlwell, M.P. Vullierme, S. Welin, D.K. Bartsch, European Neuroendocrine Tumor Society 2023 guidance paper for functioning pancreatic neuroendocrine tumour syndromes, J. Neuroendocrinol. 35 (2023) e13318.
[26] M.I. Costache, I.M. Cazacu, C.F. Dietrich, M.C. Petrone, P.G. Arcidiacono, M. Giovannini, E. Bories, J.I. Garcia, S. Siyu, E. Santo, C.F. Popescu, A. Constantin, M. S. Bhutani, A. Saftoiu, Clinical impact of strain histogram EUS elastography and contrast-enhanced EUS for the differential diagnosis of focal pancreatic masses: a prospective multicentric study, Endoscopic ultrasound 9 (2020) 116–121.
[27] P.H. Kann, Is endoscopic ultrasonography more sensitive than magnetic resonance imaging in detecting and localizing pancreatic neuroendocrine tumors? Rev. Endocr. Metab. Disord. 19 (2018) 133–137.
[28] P. Tong, D. Sun, G. Chen, J. Ni, Y. Li, Biparametric magnetic resonance imaging-based radiomics features for prediction of lymphovascular invasion in rectal cancer, BMC Cancer 23 (2023) 61.
[29] G. Parasher, M. Wong, M. Rawat, Evolving role of artificial intelligence in gastrointestinal endoscopy, World J. Gastroenterol. 26 (2020) 7287–7298.
[30] A. Eccher, F. Pagni, S. Marletta, E. Munari, A.P. Dei Tos, Perspective of a pathologist on benchmark strategies for artificial intelligence development in organ transplantation, Crit. Rev. Oncog. 28 (2023) 1–6.
[31] W. Duan, B. Xiong, T. Tian, X. Zou, Z. He, L. Zhang, Radiomics in nasopharyngeal carcinoma. Clinical medicine insights, Oncology 16 (2022) 11795549221079186.
[32] B. Chen, C. Chen, J. Wang, Y. Teng, X. Ma, J. Xu, Differentiation of low-grade astrocytoma from anaplastic astrocytoma using radiomics-based machine learning techniques, Front. Oncol. 11 (2021) 521313.
[33] T. Yang, L. Hao, R. Cui, H. Liu, J. Chen, J. An, S. Qi, Z. Li, Identification of an immune prognostic 11-gene signature for lung adenocarcinoma, PeerJ 9 (2021) e10749.
[34] W. Lu, D. Zhang, Y. Zhang, X. Qian, C. Qian, Y. Wei, Z. Xia, W. Ding, X. Ni, Ultrasound radiomics nomogram to diagnose sub-centimeter thyroid nodules based on ACR TI-RADS, Cancers 14 (2022).
[35] Y. Bian, Z. Zhao, H. Jiang, X. Fang, J. Li, K. Cao, C. Ma, S. Guo, L. Wang, G. Jin, J. Lu, J. Xu, Noncontrast radiomics approach for predicting grades of nonfunctional pancreatic neuroendocrine tumors, J. Magn. Reson. Imag. : JMRI 52 (2020) 1124–1136.
[36] C.G. Guo, S. Ren, X. Chen, Q.D. Wang, W.B. Xiao, J.F. Zhang, S.F. Duan, Z.Q. Wang, Pancreatic neuroendocrine tumor: prediction of the tumor grade using magnetic resonance imaging findings and texture analysis with 3-T magnetic resonance, Cancer Manag. Res. 11 (2019) 1933–1944.
[37] J.Y. Ye, P. Fang, Z.P. Peng, X.T. Huang, J.Z. Xie, X.Y. Yin, A radiomics-based interpretable model to predict the pathological grade of pancreatic neuroendocrine tumors, Eur. Radiol. 34 (3) (2024) 1994–2005.
[38] Y. Dong, D.H. Yang, X.F. Tian, W.H. Lou, H.Z. Wang, S. Chen, Y.J. Qiu, W. Wang, C.F. Dietrich, Pancreatic neuroendocrine tumor: prediction of tumor grades by radiomics models based on ultrasound images, Br. J. Radiol. 96 (2023) 20220783.
[39] A. Zwanenburg, M. Vallières, M.A. Abdalah, H. Aerts, V. Andrearczyk, A. Apte, S. Ashrafinia, S. Bakas, R.J. Beukinga, R. Boellaard, M. Bogowicz, L. Boldrini, I. Buvat, G.J.R. Cook, C. Davatzikos, A. Depeursinge, M.C. Desseroit, N. Dinapoli, C.V. Dinh, S. Echegaray, I. El Naqa, A.Y. Fedorov, R. Gatta, R.J. Gillies, V. Goh, M. Götz, M. Guckenberger, S.M. Ha, M. Hatt, F. Isensee, P. Lambin, S. Leger, R.T.H. Leijenaar, J. Lenkowicz, F. Lippert, A. Losnegård, K.H. Maier-Hein, O. Morin, H. Müller, S. Napel, C. Nioche, F. Orlhac, S. Pati, E.A.G. Pfaehler, A. Rahmim, A.U.K. Rao, J. Scherer, M.M. Siddique, N.M. Sijtsema, J. Socarras Fernandez, E. Spezi, R. Steenbakkers, S. Tanadini-Lang, D. Thorwarth, E.G.C. Troost, T. Upadhaya, V. Valentini, L.V. van Dijk, J. van Griethuysen, F.H.P. van Velden, P. Whybra, C. Richter, S. Löck, The image biomarker standardization initiative: standardized quantitative radiomics for high-throughput image-based phenotyping, Radiology 295 (2020) 328–338.
[40] P. Lambin, R.T.H. Leijenaar, T.M. Deist, J. Peerlings, E.E.C. de Jong, J. van Timmeren, S. Sanduleanu, R. Larue, A.J.G. Even, A. Jochems, Y. van Wijk, H. Woodruff, J. van Soest, T. Lustberg, E. Roelofs, W. van Elmpt, A. Dekker, F.M. Mottaghy, J.E. Wildberger, S. Walsh, Radiomics: the bridge between medical imaging and personalized medicine, Nat. Rev. Clin. Oncol. 14 (2017) 749–762.
[41] J. Huang, X. Xie, H. Wu, X. Zhang, Y. Zheng, X. Xie, Y. Wang, M. Xu, Development and validation of a combined nomogram model based on deep learning contrast-enhanced ultrasound and clinical factors to predict preoperative aggressiveness in pancreatic neuroendocrine neoplasms, Eur. Radiol. 32 (2022) 7965–7975.
[42] J. Gu, J. Pan, J. Hu, L. Dai, K. Zhang, B. Wang, M. He, Q. Zhao, T. Jiang, Prospective assessment of pancreatic ductal adenocarcinoma diagnosis from endoscopic ultrasonography images with the assistance of deep learning, Cancer 129 (2023) 2214–2223.
[43] X.D. Zhang, L. Zhang, T.T. Gong, Z.R. Wang, K.L. Guo, J. Li, Y. Chen, J.T. Zhang, B.G. Ye, J. Ding, J.W. Zhu, F. Liu, D.M. Hu, J. Chen, C.H. Zhou, D.W. Zou, A combined radiomic model distinguishing GISTs from leiomyomas and schwannomas in the stomach based on endoscopic ultrasonography images, J. Appl. Clin. Med. Phys. 24 (2023) e14023.
[44] C. Ricci, C. Mosconi, C. Ingaldi, G. Vara, M. Verna, I. Pettinari, L. Alberici, D. Campana, V. Ambrosini, F. Minni, R. Golfieri, R. Casadei, The 3-dimensional-computed tomography texture is useful to predict pancreatic neuroendocrine tumor grading, Pancreas 50 (2021) 1392–1399.
[45] A. Singh, J.J. Hines, B. Friedman, Multimodality imaging of the pancreatic neuroendocrine tumors, Semin. Ultrasound CT MR 40 (2019) 469–482.

[46] S. Yamada, T. Fujii, K. Suzuki, Y. Inokawa, M. Kanda, G. Nakayama, H. Sugimoto, M. Koike, S. Nomoto, M. Fujiwara, A. Nakao, Y. Kodera, Preoperative identification of a prognostic factor for pancreatic neuroendocrine tumors using multiphase contrast-enhanced computed tomography, Pancreas 45 (2016) 198–203.
[47] F. Toshima, D. Inoue, T. Komori, K. Yoshida, N. Yoneda, T. Minami, O. Matsui, H. Ikeda, T. Gabata, Is the combination of MR and CT findings useful in determining the tumor grade of pancreatic neuroendocrine tumors? Jpn. J. Radiol. 35 (2017) 242–253.
[48] M. Sugimoto, T. Takagi, T. Hikichi, R. Suzuki, K. Watanabe, J. Nakamura, H. Kikuchi, N. Konno, Y. Waragai, H. Asama, M. Takasumi, H. Watanabe, K. Obara, H. Ohira, Efficacy of endoscopic ultrasonography-guided fine needle aspiration for pancreatic neuroendocrine tumor grading, World J. Gastroenterol. 21 (2015) 8118–8124.
[49] T. Giuliani, G. Marchegiani, M.D. Girgis, S.F. Crinò, V.R. Muthusamy, L. Bernardoni, A. Pea, M. Ramera, S. Paiella, L. Landoni, A. Gabbrielli, R. Salvia, T. R. Donahue, C. Bassi, Endoscopic placement of pancreatic stent for "Deep" pancreatic enucleations operative technique and preliminary experience at two high-volume centers, Surg. Endosc. 34 (2020) 2796–2802.
[50] X. Li, F. Jiang, Y. Guo, Z. Jin, Y. Wang, Computer-aided diagnosis of gastrointestinal stromal tumors: a radiomics method on endoscopic ultrasound image, Int. J. Comput. Assist. Radiol. Surg. 14 (2019) 1635–1645.
[51] X. Geng, Y. Zhang, Y. Li, Y. Cai, J. Liu, T. Geng, X. Meng, F. Hao, Radiomics-clinical nomogram for preoperative lymph node metastasis prediction in esophageal carcinoma, Br. J. Radiol. 97 (1155) (2024) 652–659.
[52] C. Bezzi, P. Mapelli, L. Presotto, I. Neri, P. Scifo, A. Savi, V. Bettinardi, S. Partelli, L. Gianolli, M. Falconi, M. Picchio, Radiomics in pancreatic neuroendocrine tumors: methodological issues and clinical significance, Eur. J. Nucl. Med. Mol. Imag. 48 (2021) 4002–4015.
[53] H.B. Zhu, H.T. Zhu, L. Jiang, P. Nie, J. Hu, W. Tang, X.Y. Zhang, X.T. Li, Q. Yao, Y.S. Sun, Radiomics analysis from magnetic resonance imaging in predicting the grade of nonfunctioning pancreatic neuroendocrine tumors: a multicenter study, Eur. Radiol. 34 (1) (2024) 90–102.
[54] C. Liu, Y. Bian, Y. Meng, F. Liu, K. Cao, H. Zhang, X. Fang, J. Li, J. Yu, X. Feng, C. Ma, J. Lu, J. Xu, C. Shao, Preoperative prediction of G1 and G2/3 Grades in patients with nonfunctional pancreatic neuroendocrine tumors using multimodality imaging, Acad. Radiol. 29 (2022) e49–e60.
[55] F. Tixier, H. Um, R.J. Young, H. Veeraraghavan, Reliability of tumor segmentation in glioblastoma: impact on the robustness of MRI-radiomic features, Med. Phys. 46 (2019) 3582–3591.
[56] Z. Khodabakhshi, S. Mostafaei, H. Arabi, M. Oveisi, I. Shiri, H. Zaidi, Non-small cell lung carcinoma histopathological subtype phenotyping using high-dimensional multinomial multiclass CT radiomics signature, Comput. Biol. Med. 136 (2021) 104752.
[57] A. Battistella, S. Partelli, V. Andreasi, I. Marinoni, D. Palumbo, M. Tacelli, M.S. Lena, F. Muffatti, J. Mushtaq, G. Capurso, P.G. Arcidiacono, F. De Cobelli, C. Doglioni, A. Perren, M. Falconi, Preoperative assessment of microvessel density in nonfunctioning pancreatic neuroendocrine tumors (NF-PanNETs), Surgery 172 (2022) 1236–1244.
[58] P. Lohmann, K. Bousabarah, M. Hoevels, H. Treuer, Radiomics in radiation oncology-basics, methods, and limitations, Strahlenther. Onkol. : Organ der Deutschen Rontgengesellschaft ... [et al] 196 (2020) 848–855.